Atomistic structural description of the Si(001)/*a*-SiO_2 interface: The influence of different Keating-like potential parameters

Sangheon Lee, Robert J. Bondi, and Gyeong S. Hwang[a)]
Department of Chemical Engineering, University of Texas, Austin, Texas 78712, USA

(Received 6 December 2010; accepted 12 March 2011; published online 7 June 2011)

We investigate the influence of force field parameterization on the atomic-level description of the interface structure between Si(001) and its amorphous oxide [Si(001)/*a*-SiO_2] with systematic application of continuous random network model-based Metropolis Monte Carlo (CRN-MMC) simulations. Particular emphasis is given to the nature of the potentials in both the crystalline Si and *a*-SiO_2 phases, especially the quantifiable relative rigidity between phases. To assess their reliability, the energetics and mechanical properties of the interface models generated from the CRN-MMC approach with different Keating-like potential parameters were compared with those calculated using density functional theory. We statistically characterized the structural parameters and interface abruptness from various potential models of varying interface O coverage ratio in terms of bond angle, ring size, and suboxide distributions; lateral Si-O-Si bridge bond interface densities; and strain energy profiles along [001]. Comparison of our simulation results and existing experimental observations shows that a sufficiently hard character of the *a*-SiO_2 phase parameterization is essential in generation of atomically accurate depictions of the Si(001)/*a*-SiO_2 interface. © *2011 American Institute of Physics*. [doi:10.1063/1.3581110]

I. INTRODUCTION

The interface between crystalline silicon (*c*-Si) and its amorphous oxide (*a*-SiO_2) has sustained interest because of its paramount significance in electronic devices.[1] Thermal oxidation of *c*-Si is a relatively simple process that reliably produces a nearly ideal dielectric surface layer.[2] Si predominance in microelectronic applications is primarily attributed to the properties of the Si/*a*-SiO_2 interface, which is characteristically smooth and abrupt while exhibiting minimal point defect densities.[3–5] The technological significance of this semiconductor/insulator interface has propelled a long-lived, incremental effort toward a thorough understanding of its nature and properties.

Previous experimental studies have provided vital characterization of the Si(001)/*a*-SiO_2 interface. The amorphous nature of the oxide has been evidenced by transmission electron microscopy, x-ray scattering, and evaluation of infrared absorption spectra.[6–8] The interface is regarded as compositionally abrupt, comprised of only one to three monolayers (MLs) of partially oxidized Si atoms.[9–15] Photoemission experiments suggest that the suboxide distribution of Si^{1+}, Si^{2+}, and Si^{3+} states varies; ratios of 1:2:3 (Refs. 15 and 16) and 1:1:1 (Ref. 9) have been observed. The density of *a*-SiO_2 near the interface tends to be a function of annealing temperature; that is, the *a*-SiO_2 density is often higher than a typical bulk value of 2.2 g cm^{-3} during low temperature oxidation. The interface stress would be only completely relieved at elevated oxidation temperatures (>900 °C), which can be understood in terms of a viscous relaxation mechanism.[17] Preservation of an almost-perfect bonding network across the interface results in extremely low defect densities (typically between 10^{10} to 10^{12} cm^{-2}) which have been verified via electrical and electron-spin-resonance measurements.[18–20]

A parallel computational effort has driven evolution of an atomic-level description of the Si(001)/*a*-SiO_2 interface structure and facilitated investigation of its structural parameters. First-principles methods have achieved widespread acceptance for characterization of the structure and stability of Si(001)/*a*-SiO_2;[21,22] however, identification of the complex bonding configurations at the Si(001)/*a*-SiO_2 interface can be cost-prohibitive, especially when a large number of atoms are required to sample the random network of an amorphous region. As a result, computationally less expensive methods using empirical interatomic potentials, such as classical molecular dynamics (MD)[23,24] and classical Monte Carlo (MC)[25–27] simulations, frequently supplant first-principles methods to model the interface. While classical MD permits simulation of relatively large systems, time scale limitations can compromise complete structural relaxation and the availability of reliable force fields to describe bond formation/scission is also a liability.

Typical Si/SiO_2 interfaces are well represented by fully coordinated, random, tetrahedral networks in which Si and O atoms have four and two bonds, respectively. Classical MC based on a continuous random network (CRN) model[28] is a proven approach for the construction of fully relaxed, fully coordinated, tetrahedral networks of *c*-Si/*a*-SiO_2 interfaces.[25–27] During a CRN-based MC simulation, the system is relaxed via a large number of bond transpositions using Metropolis Monte Carlo (MMC) sampling,[29] where the validity of the final structure strongly depends on application of a reliable force field. Since this approach does not require description of bond formation/scission, simple and computationally less expensive valence force field (VFF) models,

[a)]Author to whom correspondence should be addressed. Electronic mail: gshwang@che.utexas.edu.

such as the three-body, harmonic Keating (KT) potential, have been widely used to facilitate the generation of ever-larger structural models.

Overall, VFF models are effective in prediction of minimum-energy configurations of fully coordinated Si-based materials when the bond lengths and angles do not significantly deviate from equilibrium;[30] however, relatively little optimization pertinent to the c-Si/a-SiO_2 interface is currently available in the literature. The previous study of Tu and Tersoff[25] based on a refined KT model generated interesting results that led to the proposal of a lateral O bridge bond as the key structural element in an ordered, ground-state interface structure. However, the bridge-bonded network structure alone cannot explain all critical experimental observations, such as Si suboxide distributions.[9,15,16,31] Recently, we optimized potential parameters for a KT model of a-SiO_x ($0 \leq x \leq 2$) based on the configurations and energies obtained from density functional theory (DFT) calculations.[32] Subsequent CRN-MMC simulations[32] demonstrated that our optimization and the optimization of Tu and Tersoff[25] for the KT potential generate nearly identical single phase (bulk) a-Si and a-SiO_2 structures; however, resultant multiphase a-SiO_x structures are notably different, indicating that the relative rigidity between a-Si and a-SiO_2 phases in multiphase structures is critical in interface structural description.

In this paper, we examine how the atomic-level description of the Si(001)/a-SiO_2 interface structure is affected by the choice of force fields with particular attention given to the soft/hard nature of the potential parameterization in each phase. First, we evaluate the accuracy of candidate VFF models for the Si(001)/a-SiO_2 interface by comparing calculated mechanical properties of resultant c-Si and a-SiO_2 regions with experimental values. Then, we perform CRN-MMC simulations based on each VFF to construct samples of Si(001)/a-SiO_2 model structures with varying interface O coverage ratios. From this set of structural samples, we evaluate the energetics generated by each potential for various Si(001)/a-SiO_2 interfaces against DFT results. We proceed to generate four independent sequences of varying O coverage ratio for larger supercells to improve statistical characterization of the resultant interface structures. We use this expanded array of interface structures to discuss the structural properties from various VFF parameterizations in terms of bond angle, ring size, and suboxide distributions; lateral Si-O-Si bridge bond interface densities; and strain energy profiles along [001]. Finally, we compare key structural parameters from our simulation results with experimental observations.

II. CALCULATION METHODS

A. Density-functional theory

All DFT calculations presented herein were performed using the Vienna ab initio simulation package (VASP)[33] within the generalized gradient approximation of Perdew and Wang (GGA-PW91).[34] Vanderbilt-type ultrasoft pseudopotentials[35] were applied to describe the interaction between ion cores and valence electrons. Valence electron wave functions were expanded using a plane wave basis set with a kinetic-energy cutoff of 400 eV. Brillouin zone sampling was accomplished with a $(2 \times 2 \times 1)$ Monkhorst–Pack k-point mesh for all Si/SiO_2 supercells. All atoms were fully relaxed using the conjugate gradient method until residual forces on constituent atoms became smaller than 5×10^{-2} eV/Å.

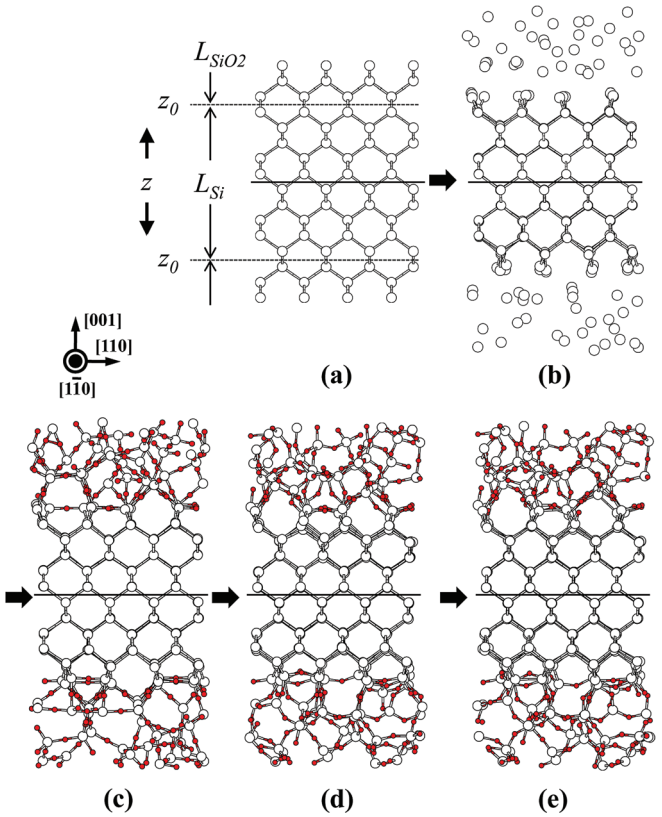

FIG. 1. (Color online) Schematic account of the five-step CRN-MMC procedure (see Sec. II C) used to construct small interface model sequences of varying O content (Γ) at the interface. The z coordinate is $\perp$ to the interface along [001]. Periodic boundary condition requirements in (a) show that each initial supercell has mirror symmetry along z about the center plane (solid line) which results in two interface planes (dashed lines) both designated as z_o. White spheres represent Si atoms and small, black (red) spheres represent O atoms.

B. Valence force fields for Si/SiO_2 interfaces

Within a VFF model, relative energetics are evaluated in terms of the increase of total energy (ΔE_{total}) with respect to the Si-Si and Si-O bond energies obtained from c-Si and c-SiO_2 (β-cristobalite in this work), respectively. ΔE_{total} can be evaluated as the sum of changes in strain energy (ΔE_{strain}) and suboxide energy (ΔE_{subox}):

$$\Delta E_{\text{total}} = \Delta E_{\text{strain}} + \Delta E_{\text{subox}}. \quad (1)$$

The suboxide (penalty) energy (ΔE_{subox}) represents an increase in Si-Si and Si-O bond energies arising from various Si suboxidation states.[36] For a given suboxide system, ΔE_{subox} is obtained by adding the suboxide penalties of partially oxidized Si atoms (Si^{1+}, Si^{2+}, and Si^{3+}). Using periodic c-SiO_x ($x = 0.5$, 1.0, 1.5) models (see Fig. 2 in Ref. 37), our DFT-GGA calculations predict suboxide energies of 0.54, 0.57, and 0.29 eV for Si^{1+}, Si^{2+}, and Si^{3+}, respectively, which corroborates previous DFT results.[36–38]

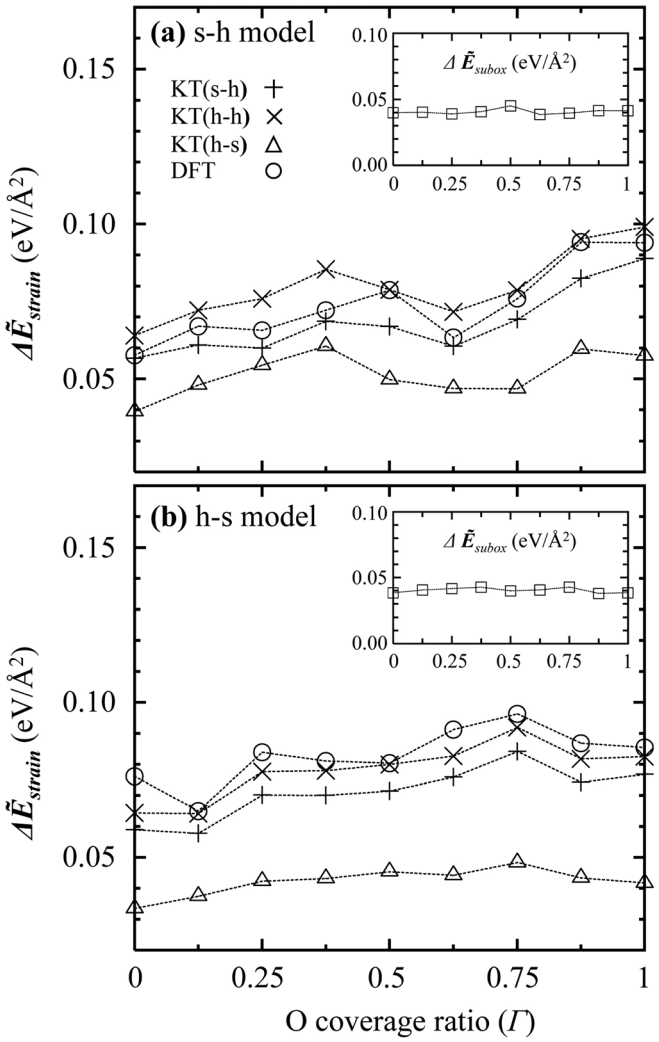

FIG. 2. Total strain (referenced to c-Si and c-SiO_2) and suboxide (insets) energies per interfacial unit area from DFT, KT(s-h), KT(h-s), and KT(h-h) calculations for (a) s-h and (b) h-s models of Si(001)/a-SiO_2 as a function of Γ. All data represents small interface structure models (initialized with $L_{Si} = 10$ and $L_{SiO_2} = 6$).

Strain energy (ΔE_{strain}) arises from lattice distortions involving bond stretching, bond angle distortion, torsion resistance, and nonbonding interactions. The structure and stability of bulk, disordered Si and SiO_2 systems have been successfully studied using a Keating-like VFF model:

$$E_{strain} = \frac{1}{2}\sum_i k_b(b_i - b_0)^2 + \frac{1}{2}\sum_{i,j} k_\theta(\cos\theta_{ij} - \cos\theta_0)^2, \quad (2)$$

where k_b (in eV/Å^2) and k_θ (in eV) refer to the bond stretching and bond angle distortion force constants, respectively, b_i and b_0 (in Å) are the lengths of the ith bond and the equilibrium (reference) bond, respectively, and θ_{ij} and θ_0 (in degrees) are the angles subtended by the ith and jth bonds (avoid double counting) and the equilibrium bond angle, respectively. The three-body, harmonic potential offers a satisfactory description of strain in Si and SiO_2 materials when the departure of bond lengths and angles from their respective equilibrium values is insignificant.[39–41]

TABLE I. Summary of Keating-like force constant optimizations and relative rigidities (γ) between c-Si and a-SiO_2 for KT(s-h) (Ref. 32), KT(h-s) Ref. 25, and KT(h-h) potentials. The k_b are expressed in eV/Å^2 and the k_θ are in eV.

	KT(s-h)	KT(h-s)	KT(h-h)
k_b(Si-Si)	9.08	9.08	9.08
k_b(Si-O)	31.39	27.00	31.39
k_θ(Si-Si-Si)	1.80	3.58	3.58
k_θ(O-Si-O)	10.25	4.32	10.25
k_θ(Si-Si-O)	4.17	3.93	4.17
k_θ(Si-O-Si)	2.62[a]	0.75	2.62[a]
γ	0.74	0.27	0.59

[a]The power of the three-body term in 2.2.

The KT potential extended by Tu and Tersoff has been widely employed to determine the atomic structure and energetics of Si/SiO_2 multiphase systems, including planar c-Si/a-SiO_2 interfaces[25,42] and oxide-embedded Si nanoparticles (np-Si/a-SiO_2).[43] In our recent work, we optimized KT potential parameters based on the configurations and energies determined from DFT calculations.[32] Table I summarizes force constant values associated with the KT potentials relevant to our present work. Table II provides equilibrium bond distances and angles used in this work.

Our optimized potential tends to over- and underestimate the energetics of a-SiO_2 and Si structures, respectively, relative to the Tu and Tersoff optimization. The higher a-SiO_2 energetics generated by our potential is largely attributed to the greater k_θ(O-Si-O) and k_θ(Si-O-Si) values (see Table I), which our previous work[32] demonstrated is essential in generating structural models with improved description of the network topology of a-SiO_2 near highly strained interfaces. In general, larger force constants produce harder potentials that result in tighter distributions of bond angles. In contrast, the propensity to underestimate Si total energies by our potential relative to that of Tu and Tersoff is mainly attributed to a smaller k_θ(Si-Si-Si) which is largely a consequence of optimizing the Si force constants using a relatively

TABLE II. Previously calculated equilibrium Si-Si and Si-O bond distances and relevant bond angles used in KT(s-h), KT(h-s), and KT(h-h) parameterizations (Ref. 32). The b_0 are given in Å and the θ_0 are in degrees.

b_0		θ_0	
Si^0-Si^0	2.362	Si-Si-Si	109.5
Si^0-Si^{1+}	2.373	O-Si-O	109.5
Si^0-Si^{2+}	2.375	Si-Si-O	109.5
Si^0-Si^{3+}	2.345	Si-O-Si	180.0
Si^{1+}-Si^{1+}	2.384		
Si^{1+}-Si^{2+}	2.385		
Si^{1+}-Si^{3+}	2.358		
Si^{2+}-Si^{2+}	2.385		
Si^{2+}-Si^{3+}	2.359		
Si^{3+}-Si^{3+}	2.335		
Si^{1+}-O	1.645		
Si^{2+}-O	1.632		
Si^{3+}-O	1.613		
Si^{4+}-O	1.593		

softer *a*-Si phase instead of *c*-Si. Note that there is a decrease in the strength of sp^3 hybridization in the tetrahedral-bonding network of *a*-Si. The smaller value of k_θ results in a wider bond angle distribution.

To emphasize this qualitative contrast in the hard/soft nature of these potentials in respective phases of the Si/SiO_2 interface model, we introduce the notation of KT(s-h) and KT(h-s) to distinguish our potential from the Tu and Tersoff potential, respectively. For example, KT(s-h) emphasizes the soft ("s") nature of the Si potential and resultant structural parameters in combination with the relatively hard ("h") character of the SiO_2 potential and structural parameters of the oxide phase. CRN-MMC simulations[32] have demonstrated that the two potentials generate nearly identical bulk *a*-Si and *a*-SiO_2 structures; however, multiphase *a*-SiO_x structures are notably different. Likewise, we expect the relative rigidity between *c*-Si and *a*-SiO_2 to be an important factor in structural determination of *c*-Si/*a*-SiO_2 interfaces.

The elastic (or Young's) modulus (Y) and bulk modulus (B) are linear and volumetric, respectively, stress/strain ratios that offer convenient metrics of elastic response.[44] We apply our previously reported moduli calculation method[44] to VFF total energy data to evaluate Y and B based on both KT(s-h) and KT(h-s) potentials for *c*-Si and *a*-SiO_2 to quantify phase rigidities. Table III provides a summary of our mechanical property calculations along with relevant experimental data for comparison. The resultant mechanical properties of the model structures are effectively determined by bulk structure selection (i.e., *c*-Si and *a*-SiO_2) for potential fitting. Previous optimization representing the KT(h-s) potential in the oxide phase can reliably model the energetics in a crystalline SiO_2 phase in which bond angle deviations are inherently miniscule; however, the sharp increase in energy for small Si-O-Si bond angles ($\theta < 150°$) is lost when applied to *a*-SiO_2 phases.[32] This soft oxide parameterization for KT(h-s) consequently results in much softer Y and B values relative to the corresponding moduli from the KT(s-h) potential. Similarly, optimization of the Si phase was based on fitting energetics to *c*-Si and *a*-Si models for KT(h-s) and KT(s-h) potentials, respectively. As shown in Table III, the softer Si parameterization for KT(s-h) consistently generates softer Y than the corresponding moduli from the KT(h-s) potential.

TABLE III. Computed average elastic (Y) and bulk (B) moduli based on KT(s-h), KT(h-s) (Ref. 25), and KT(h-h) potentials along low-index directions in *c*-Si (64 Si atoms) and for 10 independent *a*-SiO_2 (216 Si and 432 O atoms) structures. Strain was applied during mechanical property calculations using the same KT(s-h), KT(h-s), and KT(h-h) potentials used during the initial CRN-MMC simulations. Relevant experimental data is also summarized for comparison.

	Y (GPa)	**B** (GPa)	
Si <100>	122.4	89.4	KT(s-h)
	155.8	89.4	KT(h-s), KT(h-h)
	130		Ref. 51
	134		Ref. 52
Si <110>	137.5	89.4	KT(s-h)
	172.5	89.4	KT(h-s), KT(h-h)
	169		Ref. 51
	168		Ref. 52
Si <111>	142.3	89.4	KT(s-h)
	178.0	89.4	KT(h-s), KT(h-h)
	188		Ref. 51
	180		Ref. 52
a-SiO_2	98.9	40.2	KT(s-h), KT(h-h)
	46.3	21.2	KT(h-s)
	70	33.3	Ref. 53
	76.6 ± 7.2		Ref. 54
	73		Ref. 55
	73		Ref. 56
	144		Ref. 57

Overall, the harder oxide parameterization of KT(s-h) shows better agreement with experiment for *a*-SiO_2, while the harder Si parameterization of KT(h-s) exhibits somewhat better consistency with experiment for *c*-Si. As a result, this motivated us to consider another variant of the KT(s-h) potential for *c*-Si/*a*-SiO_2 where the original k_θ(Si-Si-Si) value of 1.8 eV is replaced by 3.58 eV from the KT(h-s) potential. This hybrid of the KT(s-h) and KT(h-s) potentials will be hereafter denoted as KT(h-h).

The similar B values for *c*-Si from KT(s-h) and KT(h-s) calculations can be attributed to nearly identical k_b values for the two potentials, suggesting that B is insensitive to Si-Si-Si bond angle distortions. The remaining disparities for Y and B in both phases from the KT(s-h) and KT(h-s) potentials can be explained by the aforementioned differences in k_b and k_θ.

Since both bond (Si-Si and Si-O) stretching and angle (Si-Si-Si, O-Si-O, and Si-O-Si) distortion contribute to Y for *c*-Si and *a*-SiO_2, we quantify the relative rigidity between phases using Y, rather than B. We introduce the following dimensionless quantity as a measure of relative rigidity:

$$\gamma = \frac{Y_{a\text{-}SiO_2}}{Y_{c\text{-}Si}}, \tag{3}$$

where $Y_{c\text{-}Si}$ and $Y_{a\text{-}SiO_2}$ are the bulk Young's moduli for *c*-Si and *a*-SiO_2, respectively. $Y_{c\text{-}Si}$ is inherently anisotropic, so we use an average $Y_{c\text{-}Si}$ over three low-index directions for the sake of simplicity. A more rigorous evaluation of the *c*-Si/*a*-SiO_2 interface structure would require distinct treatment of each *c*-Si orientation. As shown in Table III, $Y_{c\text{-}Si}$ along <111> is the most rigid, so increasing the Si phase rigidity by increasing k_θ(Si-Si-Si) is likely an appropriate adjustment to the VFF parameter set. In the present work, Si phase rigidity optimized using *a*-Si should be adequate since $Y_{c\text{-}Si}$ along <100> is relatively soft and similar to typical values of $Y_{a\text{-}Si}$ (Refs. 32, 45, 46). Our calculations show that *c*-Si ($Y_{c\text{-}Si} = 168.8$ GPa) from either KT(h-s) or KT(h-h) is more rigid than *c*-Si ($Y_{c\text{-}Si} = 134.1$ GPa) from KT(s-h). In contrast, *a*-SiO_2 ($Y_{a\text{-}SiO_2} = 46.3$ GPa) from KT(h-s) is far less rigid than *a*-SiO_2 ($Y_{a\text{-}SiO_2} = 98.9$ GPa) from KT(s-h) or KT(h-h). From Eq. (3), we obtain $\gamma_{KT(s\text{-}h)} = 0.74$, $\gamma_{KT(h\text{-}s)} = 0.27$, and $\gamma_{KT(h\text{-}h)} = 0.59$ for the KT(s-h), KT(h-s), and KT(h-h) potentials, respectively, as summarized in Table I.

C. MC simulations for interface structure generation

For CRN-MMC simulations, the resultant structural properties of the Si(001)/*a*-SiO_2 interface correlates with the

initial O content present. As a result, we constructed multiple models of varying O content at the interface using the procedure depicted in Fig. 1 and described in the five steps enumerated below to evaluate the structural characteristics of the interface:

(1) We started with a $16 \times (L_{Si} + L_{SiO_2})$-atom periodic Si supercell with one {100} facet and two {110} facets, i.e., the supercell consists of $(L_{Si} + L_{SiO_2})$ Si MLs along the [001] direction and each ML has 4×4 periodicity along the two <110> directions as depicted in Fig. 1(a). Here, L_{SiO_2} and L_{Si} denote the number of Si layers along the [001] direction to be oxidized and to remain unoxidized, respectively.

(2) Assuming that O atoms are incorporated into Si-Si bonds in L_{SiO_2} consecutive Si layers, the supercell is stretched along [001] to fulfill the new volume $V = V_{Si} \times (N_{Si} - N_O/2) + V_{SiO_2} \times N_O/2$, where N_{Si} and N_O denote the number of Si and O atoms, respectively, and V_{Si} and V_{SiO_2} denote the unit volumes of a-Si and a-SiO_2, respectively. V_{Si} and V_{SiO_2} are extracted from corresponding densities of 2.28 g cm^{-3} and 2.2 g cm^{-3}, respectively.[47,48] Then, the L_{SiO_2} Si layers are sequentially relaxed into amorphous states by MC bond-switching moves at temperatures of 10^4 and 3000 K with $10 \times 16 \times L_{SiO_2}$ and $100 \times 16 \times L_{SiO_2}$ trials of bond-switching moves, which results in an intermediate model with unrealistic a/c interfaces [Fig. 1(b)]. Here, the equilibrium Si-Si bond length within L_{SiO_2} Si layers is temporarily set to $b_0 = 3.1$ Å, assuming that the amorphized region will eventually be oxidized.

(3) O atoms are incorporated into Si-Si bonds in the L_{SiO_2} amorphized Si layers of the intermediate model, resulting in an intermediate Si(001)/a-SiO_2 interface model as depicted in Fig. 1(c). From this intermediate model, eight more intermediate models with varying O content were prepared by methodically inserting batched increments of eight O atoms (four O atoms to the top interface paired with four O atoms to the bottom interface) into Si-Si bonds at the interface, while the supercell was simultaneously expanded along [001] to compensate for the additional atoms. Insertion sites were chosen randomly with the objective of saturating Si-Si bonds with O near the interface.

(4) Each configuration was relaxed by bond-switching maneuvers within the oxide phase (excluding all Si^0 atoms) in a thermal sequence of 5000, 4000, 3000, 2000, and 1000 K with approximately $200 \times N_{Si}$ trials in each temperature stage, where N_{Si} denotes the number of Si atoms [Fig. 1(d)].

(5) Finally, each configuration was relaxed via bond-switching maneuvers throughout the supercell (both phases) in consecutive thermal stages of 3000, 2000, and 1000 K over approximately $200 \times N_{Si}$ trials for each temperature [Fig. 1(e)].

Each time the simulation temperature changed, the lowest-energy configuration from the prior simulation was adopted as the initial configuration for the subsequent simulation stage. In order to improve efficiency of the overall MC simulation, we prioritized atoms with atomic strain energy greater than half the mean of the entire system for earliest selection. This systematic approach provides a thorough description of layer by layer oxidation near the Si(001)/a-SiO_2 interface. During steps 4 and 5, the volume of the supercell was allowed to relax along [001]. For the sake of convenience, we define an O coverage ratio (Γ) over an interval from 0 to 1 in 0.125 increments (corresponding to the addition of eight O atoms) to distinguish the nine interface models with variable O content.

For MMC simulations, we included an additional repulsive term (E_r) in ΔE_{total} to effectively prevent nonbonded atoms from interacting.[25,39] Inclusion of E_r is particularly important in a-SiO_x topological determination, likely because the flexible Si-O-Si linkages permit much more structural degrees of freedom than fourfold-coordinated a-Si. The repulsive contribution is given as follows:

$$E_r = k_r \sum_{mn} (d_2 - r_{mn})^3, \tag{4}$$

where m and n denote atoms which are neither 1st nor 2nd neighbors in the network, r_{mn} is the distance between two atoms (evaluated only for $r_{mn} < d_2$), and d_2 is a cutoff distance. We applied the following parameters to Eq. (4): d_2(Si-Si) = 3.84 Å, d_2(Si-O) = 3.2 Å, d_2(O-O) = 2.61 Å, and $k_r = 0.5$ eV/$Å^3$ from consideration of Refs. 39 and 40. The E_r term becomes negligible for the well-relaxed Si(001)/a-SiO_2 models presented in this paper.

III. RESULTS AND DISCUSSION

A. Comparison to DFT energetics

We evaluated the reliability of the KT(s-h), KT(h-s), and KT(h-h) potentials for the energetics of Si(001)/a-SiO_2 interfaces by comparison with DFT results. We prepared small model structures (see Fig. 1) for Si(001)/a-SiO_2 using MC simulations pairing the contrasting extremes of rigidity in each phase through application of the KT(s-h) and KT(h-s) potentials. Starting from a Si supercell with $L_{Si} = 10$ and $L_{SiO_2} = 6$, we followed the aforementioned procedure (Section II C) to prepare a sequence of interface models with Γ varying from 0 ($L_{Si} = 10$ and $L_{SiO_2} = 6$) to 1 ($L_{Si} = 8$ and $L_{SiO_2} = 8$). The two different structural models based on KT(s-h) and KT(h-s) potentials will be denoted as s-h and h-s models, respectively, throughout the discussion.

Figure 2(a) shows the variations of $\Delta\tilde{E}_{strain}$ and $\Delta\tilde{E}_{subox}$ (per interfacial unit area) from DFT, KT(s-h), KT(h-s), and KT(h-h) calculations for the s-h structure models as a function of Γ. While no appreciable difference in suboxide energies is evident [Fig. 2(a) inset] as a function of Γ, significant differences arise in the strain energies. Overall, KT(s-h) and DFT provide reasonable agreement, while KT(h-h) tends to slightly overestimate $\Delta\tilde{E}_{strain}$. This reaffirms our earlier assertion that a soft Si phase parameterization based on a-Si is appropriate for the relatively soft Si(001) interface, whereas a harder Si phase parameterization is likely suitable for a more rigid interface orientation, such as Si(111).

Likewise, Fig. 2(b) shows the variation of $\Delta\tilde{E}_{strain}$ and $\Delta\tilde{E}_{subox}$ for the h-s model structures. While the overall trend

is similar to the s-h models, KT(s-h) tends to underestimate $\Delta\tilde{E}_{\text{strain}}$ relative to DFT. KT(h-h) also slightly underestimates $\Delta\tilde{E}_{\text{strain}}$ while showing slightly better agreement with DFT than KT(s-h). For both s-h and h-s models, KT(h-s) yields consistently smaller $\Delta\tilde{E}_{\text{strain}}$ values compared to KT(s-h), KT(h-h), and DFT. This can be anticipated because lattice strain in the a-SiO_2 region is significantly underestimated by the KT(h-s) potential. Note that KT(h-h) and KT(h-s) should be relatively accurate in evaluating $\Delta\tilde{E}_{\text{strain}}$ of c-Si under minor strain [see narrow Si-Si-Si angle distribution in Fig. 3(a)], but their k_θ(Si-Si-Si) are too high for c-Si under significant strain [see broad Si-Si-Si angle distribution in Fig. 3(a)]. This can be inferred from consideration of the increased Si-Si-Si bond angle pliability as it deviates further from equilibrium; we observe that the KT(s-h) potential underestimates $Y_{c\text{-Si}}$ despite its relatively accurate estimation of $\Delta\tilde{E}_{\text{strain}}$ and Y for a-Si. These calculation results suggest that a k_θ(Si-Si-Si) value intermediate of those applied for KT(s-h) ($=1.80$ eV) and KT(h-h) ($=3.58$ eV) may extend agreement with DFT results.

We also compared structural descriptions of Si(001)/a-SiO_2 interfaces based on bond angle distributions. Bond lengths (Si-Si and Si-O) in a-SiO_x materials are largely a function of Si oxidation state, but the small bond length variations have little influence on the structural topology of the Si/SiO_2 system.[32] The Si-O-Si bond angle distribution is a critical quantity for the description of the bonding network of a-SiO_x; variation in this structural parameter is considered to be one of the main sources of disorder in a-SiO_x ($x>0$).

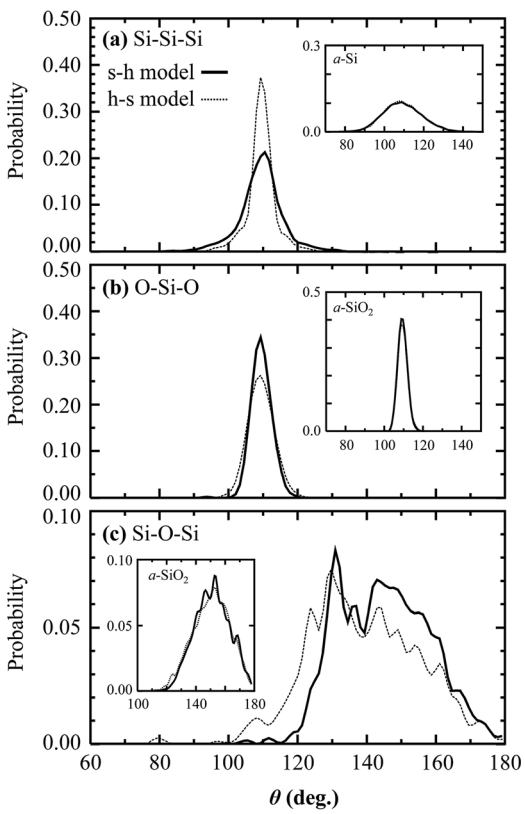

FIG. 3. (a) Si-Si-Si, (b) O-Si-O, and (c) Si-O-Si bond angle distributions averaged over $0\le\Gamma\le0.875$ for the s-h and h-s interface models of Si(001)/a-SiO_2. All data represents small interface structure models (initialized with $L_{\text{Si}}=10$ and $L_{\text{SiO}_2}=6$). In the insets, bulk counterpart distributions representing ten independent a-Si (216 Si atoms) and a-SiO_2 (216 Si and 432 O atoms) models are also provided.

In Fig. 3, we present relevant bond angle distributions of the s-h and h-s models ($0\le\Gamma\le0.875$) along with their bulk counterparts for reference. Note that the bond topology and strain energy of amorphous silica-based materials are mainly determined by the three-body contributions in Eq. (2). Average values and standard deviations of the bond angle distributions are reported in Table IV. For Si-Si-Si [Fig. 3(a)], three layers of Si atoms (Si^0 oxidation state) closest to the top and bottom interfaces are represented (six total layers), where six bond angles are associated with each Si atom. For O-Si-O [Fig. 3(b)], three layers of Si atoms (Si^{4+} oxidation state) closest to the top and bottom interfaces are represented (six total layers), where six O-Si-O bond angles are associated with each Si atom. For Si-O-Si [Fig. 3(c)], all Si-O-Si bond angles whose constituent Si atoms were selected for O-Si-O bond angle analysis are represented.

The s-h models exhibit a Si-O-Si distribution ranging from 110° to 180° with an average angle (standard deviation) of 144.7° (9.2°). Compared to the s-h models, the h-s models show a broader bond angle distribution extending from 100° to 180°, where a notable contribution from smaller bond angles results in an average Si-O-Si angle (standard deviation) of only 138.8° (11.1°). Likewise, the h-s models also show a slightly broader distribution of O-Si-O bond angles than the s-h models. In contrast, the s-h models exhibit a broader distribution of Si-Si-Si bond angles than the h-s models. In the insets, we observe that the three reference bond angle distributions from bulk a-Si and a-SiO_2 exhibit few discrepancies between s-h and h-s models and are consistent with experiment.

Compared to the bulk references, the discussed discrepancies among the three bond angle distributions between the s-h and h-s models indicate strong interplay in lattice strain between phases across the interface. Our results clearly demonstrate that the relative rigidity of a-SiO_2 to c-Si is essential in structural determination of Si(001)/a-SiO_2 interfaces. The smaller $\gamma_{\text{KT(h-s)}}$ suggests that the KT(h-s) potential will generate an excessively pliable a-SiO_2 phase that permits

TABLE IV. Average values and standard deviations given in () of Si-Si-Si, O-Si-O, and Si-O-Si bond angle distributions (data is visually depicted in Fig. 3) averaged over $0\le\Gamma\le0.875$ for the s-h and h-s interface models of Si(001)/a-SiO_2. All data represents small interface structure models (initialized with $L_{\text{Si}}=10$ and $L_{\text{SiO}_2}=6$). For the sake of reference, experimental data for bulk a-Si and a-SiO_2 is also provided.

		s-h	h-s	Experiment
Si(001)/a-SiO_2	Si-Si-Si	109.3 (4.6)	109.4 (2.8)	
	O-Si-O	109.4 (2.1)	109.4 (2.7)	
	Si-O-Si	144.7 (9.2)	138.8 (11.1)	
a-Si	Si-Si-Si	109.2 (10.0)	109.3 (9.8)	109.5 (9.63)[a]
				109.5 (10.5)[b]
a-SiO2	O-Si-O	109.5 (2.3)	109.5 (2.5)	
	Si-O-Si	151.5 (12.0)	151.1 (12.7)	151 (11.0)[c]

[a]Reference 58 (Thermally annealed a-Si).
[b]Reference 58 (As-implanted a-Si).
[c]Reference 59 (DFT interpretation for NMR).

disproportionate lattice distortion on the oxide side of the interface. In contrast, the larger $\gamma_{KT(s\text{-}h)}$ implies that the KT(s-h) potential will yield a relatively more rigid a-SiO_2 phase that resists excessive lattice distortion from lattice mismatch between phases. This provides a plausible explanation for the disparate bond angle distributions of the s-h and h-s interface models in Fig. 3.

B. Interface atomic structures: Comparison of different KT potentials

We continued investigation of the Si(001)/a-SiO_2 interface structural sensitivity to KT potential parameterization by constructing larger interface models where the dimension along [001] is expanded for statistical structure sampling. Starting with an initial Si supercell with $L_{Si} = 36$ and $L_{SiO_2} = 12$, we used the aforementioned procedure (Sec. II C) to prepare four independent sequences (O coverage ratio) of interface models generated with KT(s-h), KT(h-s), and KT(h-h) potentials. Extending the scope of the small interface model characterization, we will discuss the structural properties of these three models (s-h, h-s, and h-h) in terms of bond angle distributions, ring size distributions, Si oxidation state statistics, and lateral Si-O-Si bridge bond interface densities.

1. Bond angle distributions

In Fig. 4, we present the (a) Si-Si-Si, (b) O-Si-O, and (c) Si-O-Si bond angle distributions for the s-h, h-s, and h-h models. Their averages and standard deviations are reported in Table V. While the three bond angle distributions of the s-h and h-s models exhibit similar trends to those shown in Fig. 3 for the small interface models, the additional distributions of the h-h models are intuitively intermediate to those of the s-h and h-s models, especially for the Si-Si-Si distributions. For the O-Si-O and Si-O-Si bond angle distributions, the h-h distributions are nearly equivalent to those of s-h model distributions since both share the hard oxide parameterization. This indicates that rigidity modulation in the a-SiO_2 phase is more likely to distort bond angles in the c-Si phase than a change in c-Si phase rigidity will modify bond angles in the a-SiO_2 phase.

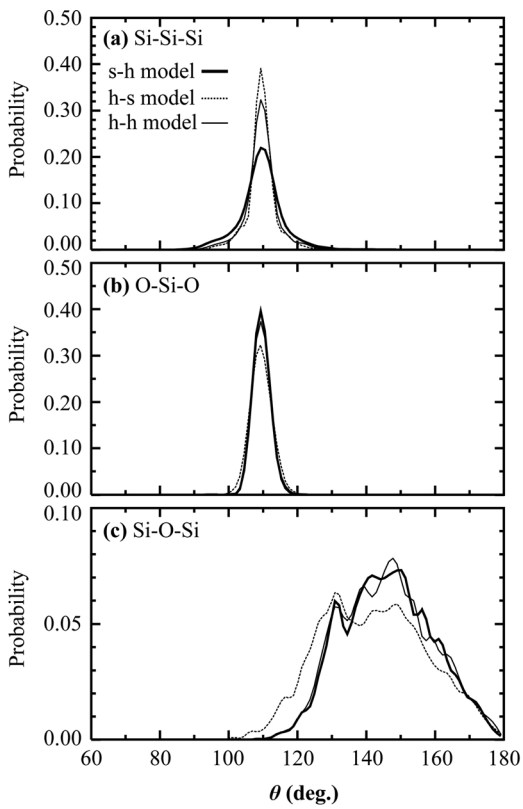

FIG. 4. (a) Si-Si-Si, (b) O-Si-O, and (c) Si-O-Si bond angle distributions averaged over $0 \leq \Gamma \leq 0.875$ for four independent sequences of s-h, h-s, and h-h interface models of Si(001)/a-SiO_2. All data represents large interface structure models (initialized with $L_{Si} = 36$ and $L_{SiO_2} = 12$).

TABLE V. Average values and standard deviations given in () of Si-Si-Si, O-Si-O, and Si-O-Si bond angle distributions (data is visually depicted in Fig. 4) averaged over $0 \leq \Gamma \leq 0.875$ for four independent sequences of s-h, h-s, and h-h interface models of Si(001)/a-SiO_2. All data represents large interface structure models (initialized with $L_{Si} = 36$ and $L_{SiO_2} = 12$).

	s-h	h-s	h-h
Si-Si-Si	109.3 (4.6)	109.4 (2.9)	109.4 (3.4)
O-Si-O	109.5 (1.8)	109.4 (2.2)	109.4 (1.9)
Si-O-Si	146.0 (9.0)	141.8 (10.6)	145.7 (9.2)

2. Ring size distributions

In Fig. 5, we present the ring size distributions for the a-SiO_2 components of the s-h, h-s, and h-h models. Here, ring size distributions are computed using a shortest path analysis in which all bond angles of each Si atom are evaluated by determination of the shortest path of Si atoms to complete a ring.[49] For a-SiO_2, the algorithm only considers paths comprised solely of Si^{4+} atoms as rings (O atoms are not

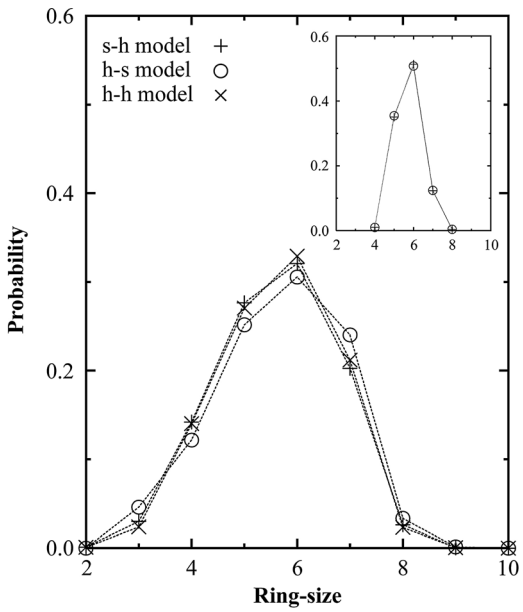

FIG. 5. Ring size distributions for the a-SiO_2 phases of s-h, h-s, and h-h interface models of Si(001)/a-SiO_2. All data represents large interface structure models (initialized with $L_{Si} = 36$ and $L_{SiO_2} = 12$). In the inset, distributions representing ten independent s-h and h-s models of bulk a-SiO_2 (216 Si and 432 O atoms) are also provided.

counted); for comparison, the ring size distributions for bulk a-SiO_2 structures are also provided (Fig. 5 inset). The a-SiO_2 phase in the interface models yields broader ring size distributions than in bulk a-SiO_2 for either s-h or h-s models. This indicates that the a-SiO_2 phase near the interface is more strained than bulk a-SiO_2. We also notice in the a-SiO_2 phase that the h-s models generally exhibit broader ring size distributions than either s-h or h-h models; the discrepancies between the s-h and h-h models are negligible. This is consistent with the trend observed in the bond angle distributions. The feasibility of generating excessively strained a-SiO_2 phases in the h-s models is not surprising considering that $\gamma_{KT(h\text{-}s)}$ ($=0.27$) is much smaller than either $\gamma_{KT(s\text{-}h)}$ ($=0.74$) or $\gamma_{KT(h\text{-}h)}$ ($=0.59$).

3. Suboxide characterization

In Fig. 6, we present the variation of Si suboxide state (Si^{1+}, Si^{2+}, Si^{3+}) atomic interface densities as a function of Γ for (a) s-h, (b) h-s, and (c) h-h models as well as their mean atomic densities ($\bar{N}_{subox}$) over $0 \le \Gamma \le 0.875$ (0 and 1 are effectively identical because of <001> periodicity). For each model, we define a nominal interface position, z_0, that effectively defines a reference for the Si(001)/a-SiO_2 interface,

$$z_0 = \frac{\sum z(Si^{1+}) + \sum z(Si^{2+})}{n(Si^{1+}) + n(Si^{2+})}, \tag{5}$$

where $z(Si^m)$ is the distance of a Si atom with oxidation state m from the center plane (illustrated in Fig. 1) of the c-Si region along [001], $n(Si^m)$ is the number of Si^m, and the summations are conducted overall four independent samples. The Si^{1+} and Si^{2+} states can be interpreted as interface Si atoms of the c-Si phase with one and two O neighbors, respectively. The statistics illustrated in Fig. 6 only consider Si atoms with $[z(Si^m) - z_0] < 5$ Å. The interface density of each suboxide state is significantly different between the s-h and h-s models. In the s-h models, Si suboxide states are distributed across Si^{1+}, Si^{2+}, and Si^{3+} states in the ratio of 1:1.4:1.9, where the total suboxide interface density averaged overall Γ [$\Sigma\bar{N}_{subox} = (Si^{1+} + Si^{2+} + Si^{3+})/nm^2$] is 8.9 nm^{-2} ($=1.31$ ML). Interestingly, in the h-s models, the Si^{2+} state prevails and yields a distribution (Si^{1+}:Si^{2+}:Si^{3+}) of 1:4.7:2.0, where $\Sigma\bar{N}_{subox}$ is 8.0 nm^{-2} ($=1.18$ ML). For the h-h model, we observe a distribution (Si^{1+}:Si^{2+}:Si^{3+}) of 1:1.9:1.4, where $\Sigma\bar{N}_{subox}$ is 8.9 nm^{-2} ($=1.31$ ML). In addition, the h-h model also exhibits inverse behavior between Si^{2+} and Si^{3+} populations with respect to Γ (Si^{2+} is minimum and Si^{3+} is maximum for $\Gamma \approx 0.5$), while Si^{1+} is notably less sensitive to Γ. Photoemission experimental results vary; the suboxide distribution (Si^{1+}:Si^{2+}:Si^{3+}) is 1:2:3 from Refs. 15 and 16 and 1:1:1 from Ref. 9. The s-h model suboxide distributions are not dominated by the Si^{2+} state; so they likely provide better agreement with experimental results than the h-h and h-s models.

The suboxide distributions suggest that the s-h and h-h models should yield more graded Si/SiO_2 interface profiles than the h-s models. Experimental studies also support somewhat graded interface profiles containing up to three monolayers of Si suboxide, rather than the ideally abrupt interface.[9–15] Formation of abrupt Si/SiO_2 interfaces is driven by suboxide penalty minimization, but is simultaneously mitigated by increasing lattice distortions during phase separation. The

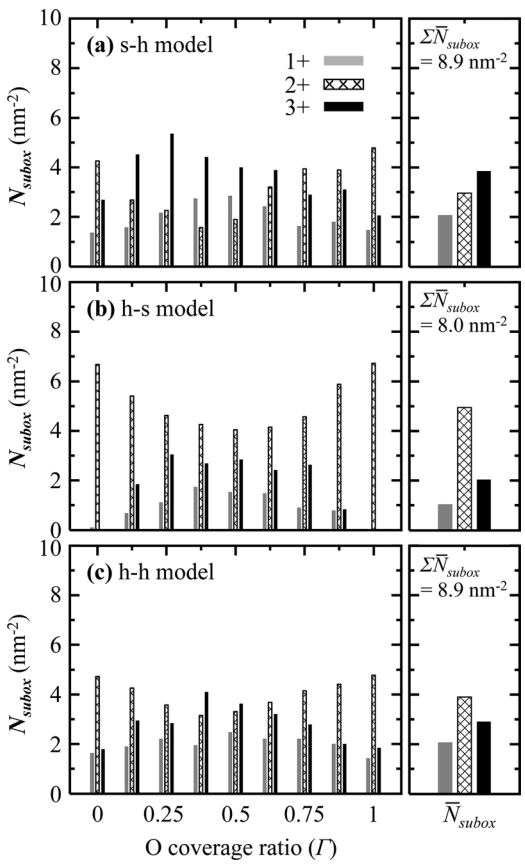

FIG. 6. Si suboxide distributions (Si^{1+}, Si^{2+}, and Si^{3+}) per interfacial unit area as a function of Γ for (a) s-h, (b) h-s, and (c) h-h interface models of Si(001)/a-SiO_2. All data represents large interface structure models (initialized with $L_{Si} = 36$ and $L_{SiO_2} = 12$). The right panels illustrate mean suboxide distributions averaged over $0 \le \Gamma \le 0.875$ together with respective total suboxide interface densities ($\Sigma\bar{N}_{subox}$).

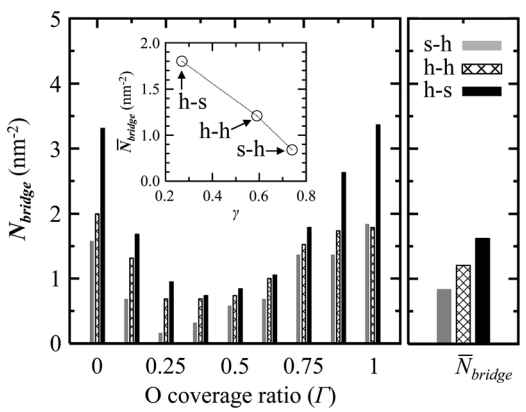

FIG. 7. Lateral Si-O-Si bridge bonds (N_{bridge}) per interfacial unit area as a function of Γ for s-h, h-s, and h-h interface models of Si(001)/a-SiO_2. All data represents large interface structure models (initialized with $L_{Si} = 36$ and $L_{SiO_2} = 12$). The right panel illustrates mean bridge bond interface densities averaged over $0 \le \Gamma \le 0.875$ for each structure model. The inset plots values of $\bar{N}_{bridge}$ from the right panel as a functional of relative rigidity (γ) between a-SiO_2 and c-Si.

hard oxide character of the s-h and h-h parameterizations tempers phase separation by raising the associated strain contribution; in consequence, more graded interface profiles occur in the s-h and h-h models relative to the h-s models.

4. Lateral bridge bond interface densities

In Fig. 7, we present the variation in interface densities of lateral Si-O-Si bridge bonds (N_{bridge}) as a function of Γ for the s-h, h-s, and h-h models as well as their mean values ($\bar{N}_{\text{bridge}}$) over $0 \leq \Gamma \leq 0.875$. For the sake of convenience, we count O atoms between two Si^{2+} atoms as bridging O atoms. Over nearly the entire range of Γ, the degree of lateral Si-O-Si bridge bonding in the s-h models ($\bar{N}_{\text{bridge}} = 0.84\ \text{nm}^{-2}$) is smaller than that observed in either the h-s models ($\bar{N}_{\text{bridge}} = 1.8\ \text{nm}^{-2}$) or h-h models ($\bar{N}_{\text{bridge}} = 1.21\ \text{nm}^{-2}$). In particular, at the limiting cases of $\Gamma = 0$ and 1, the h-s models have lateral Si-O-Si bridge bond interface coverage exceeding 90% (or $N_{\text{bridge}} = 3.0\ \text{nm}^{-2}$), in good agreement with the results of Tu and Tersoff,[25] whereas the s-h and h-h models exhibit much less lateral Si-O-Si bridge bond interface coverage. In addition, the inset of Fig. 7 also shows that $\bar{N}_{\text{bridge}}$ decreases with increasing relative rigidity (γ).

C. Strain profile comparison of different interface models

We investigated the strain energy along [001] by constructing strain energy profiles along the z coordinate using the s-h, h-h, and h-s models. Recall that the h-s model shows a more abrupt interface than the s-h and h-h models. In addition, we generated another large interface model with the KT(s-h) potential, s-h*, as a fourth model to exemplify an ideally abrupt interface; although physically unfavorable,[50] the s-h* model provides a convenient limiting case for reference. Unlike the other interface models, we used constrained MC simulations (steps 1 through 4 in Section II C) to ensure all interface Si atoms in s-h* retained Si^{2+} oxidation states with $\Gamma = 1$.

Figure 8 provides the strain energy profiles for the four interface model structures with energetics computed using the (a) KT(s-h), (b) KT(h-s), and (c) KT(h-h) potentials with reference to their respective bulk a-SiO_2 strain energies. All strain energies are given relative to c-Si and c-SiO_2 (β-cristobalite) and provided on a per Si atom basis ($\Delta\hat{E}_{\text{strain}}$) to remove the influence of density variation. The strain energy profiles, averaged over $0 \leq \Gamma \leq 0.875$ for the s-h, h-s, and h-h models, are calculated on a Si ML basis along [001]. Each designated ML consists of 32 Si atoms (16 atoms from both the top and bottom interfaces) and their neighboring O atoms, where the ML position (z) is computed by averaging the z distances of the 32 Si atoms from the center plane of the c-Si region along [001].

It is evident in Fig. 8 that $\Delta\hat{E}_{\text{strain}}$ is notably lower for the KT(h-s) potential than either the KT(s-h) or KT (h-h) potentials, especially in comparison of the oxide phases. In addition, it is apparent that $\Delta\hat{E}_{\text{strain}}$ in the oxide regions is notably higher for the more abrupt interfaces (h-s and s-h*) relative to the more graded s-h and h-h interfaces from both Figs. 8(a) and (c); in contrast, $\Delta\hat{E}_{\text{strain}}$ in the oxide region

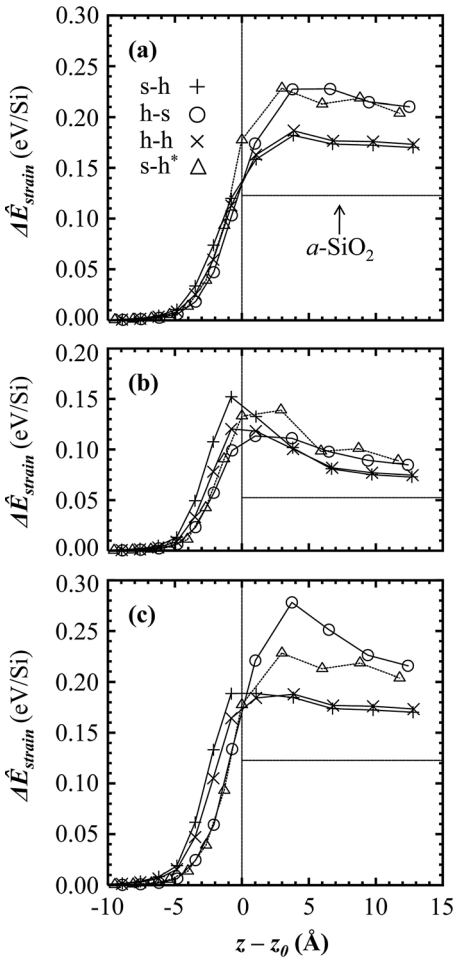

FIG. 8. Strain energy profiles computed for the s-h, h-s, h-h, and ideally abrupt (s-h*) interface models of Si(001)/a-SiO_2 using (a) KT(s-h), (b) KT(h-s), and (c) KT(h-h) potentials to calculate strain energies [referenced to c-Si and c-SiO_2 (β-cristobalite)] on a per Si atom basis along the z coordinate [001]. Each data point represents the average over $0 \leq \Gamma \leq 0.875$ for the s-h, h-s, and h-h models and at $\Gamma = 1$ for the s-h* model; all the structure models were initialized with $L_{Si} = 36$ and $L_{SiO_2} = 12$. The nominal interface (z_o) and bulk a-SiO_2 strain energies calculated with respective potentials are provided for reference with solid lines.

for Fig. 8(b) does not vary significantly among any of the four interface models. This reinforces that the soft parameterization of the oxide phase for KT(h-s) calculations is overly insensitive to structural distortion. Conversely, albeit less significant, the rigid parameterization of the Si phase using either KT(h-s) or KT(h-h) potentials better distinguishes the four interface models than the softer Si phase described by KT(s-h) parameterization. Interestingly, the KT(h-h) energetic calculations applied to the h-s model actually show higher $\Delta\hat{E}_{\text{strain}}$ in the near-interface oxide than that exhibited by the ideally abrupt model, s-h*. It also appears characteristic for KT(h-s) calculations, irrespective of interface model, to produce maximum $\Delta\hat{E}_{\text{strain}}$ closer to the nominal interface relative to KT(s-h) and KT(h-h) calculations.

In Fig. 8(a), it is apparent that the strain profile of the ideally abrupt interface (s-h*) has a steeper slope than exhibited by the s-h model in the near-interface Si region; in consequence, $\Delta\hat{E}_{\text{strain}}$ for s-h* is briefly lower ($-5\ \text{Å} \leq z - z_o \leq -1\ \text{Å}$), but ultimately much higher ($-1\ \text{Å} < z - z_o$) than $\Delta\hat{E}_{\text{strain}}$

for the s-h model in the interface vicinity. The general trend of lower $\Delta\hat{E}_{\text{strain}}$ values in the *c*-Si regions paired with higher $\Delta\hat{E}_{\text{strain}}$ values in the *a*-SiO_2 regions for the abrupt interfaces (h-s and s-h*) compared to the graded interfaces (s-h and h-h) persists for all three energetic calculations. Not surprisingly, the KT(h-h) calculations [Fig. 8(c)] best sharpen the contrasting strain profiles between the abrupt and relatively graded interface models. Experimental measurements also support the favorability of more graded interface profiles. The ion scattering investigation of Ref. 50 found Si atom displacements larger than 0.09 Å penetrating three layers deep into the Si substrate, ruling out an ideally abrupt transition with regularly ordered O bridge bonds. As a result, the more-strained *c*-Si side exhibited by the s-h models provides better consistency with ion scattering measurements.

The CRN-MMC approach with a simple VFF model can provide a reasonable description of the defect free, minimum energy configurations of various Si/SiO_2 composite systems, which will further allow thorough studies of their optical and electrical properties and also the nature and behavior of defects and impurities in the complex system. However, the Si/SiO_2 interface structure would also be influenced by process conditions; for instance, a significant amount of compressibility can be found in the SiO_2 region near the interface during oxidation of Si nanowires, when the rate of oxidation is greater than the rate of structural relaxation.[60] In those cases, not only thermodynamic equilibrium but also kinetics might need to be considered. Moreover, the Si/SiO_2 interface often contains a non-negligible amount of coordination defects due largely to lattice-mismatch-induced strains. To take into account the kinetic effect, it would be necessary to use more advanced methods such as molecular dynamics with a more sophisticated potential model.[23,24,61,62]

IV. SUMMARY

We investigate the effect of different valence force field (VFF) parameter optimizations on the atomic-level description of the Si(001)/*a*-SiO_2 interface structure with particular emphasis given to the soft/hard nature of the potential parameterization in each phase. Two Keating-like (KT) VFF models pairing the contrasting extremes of rigidity [soft ("s") and hard ("h")] in each phase provided a basis for our study: (1) KT(s-h), which we previously optimized[32] for *a*-SiO_x ($0 \leq x \leq 2$), corresponds to a soft Si phase paired with a harder oxide phase; and (2) KT(h-s), which was previously optimized in Ref. 25, corresponds to a hard Si phase paired with a softer oxide phase. Since the KT(s-h) and KT(h-s) potentials generate nearly identical bulk *a*-Si and *a*-SiO_2 structures, but notably different interface structures, the degree of rigidity in each phase was identified as an essential factor in interface structural description.

We evaluated Young's modulus for each potential for *c*-Si and *a*-SiO_2 to quantify the rigidity in respective phases. Overall, the harder oxide parameterization of KT(s-h) shows better agreement with experimental data for *a*-SiO_2, while the harder Si parameterization of KT(h-s) exhibits somewhat better consistency with experiment for *c*-Si. This observation prompted consideration of another VFF variant, denoted as KT(h-h), in which the KT(s-h) potential was modified by substitution of the soft k_θ(Si-Si-Si) value of 1.8 eV with 3.58 eV from the KT(h-s) potential. To quantify relative rigidity, we introduced a dimensionless quantity: $\gamma = Y_{a\text{-}SiO_2}/Y_{c\text{-}Si}$, where $Y_{c\text{-}Si}$ and $Y_{a\text{-}SiO_2}$ are the bulk phase Young's moduli for *c*-Si and *a*-SiO_2, respectively. For the various potentials, we obtained $\gamma_{KT(s\text{-}h)} = 0.74$, $\gamma_{KT(h\text{-}s)} = 0.27$, and $\gamma_{KT(h\text{-}h)} = 0.59$. The small $\gamma_{KT(h\text{-}s)}$ value indicates that the KT(h-s) potential generates an excessively pliable *a*-SiO_2 phase that permits excessive lattice distortion; in contrast, the larger $\gamma_{KT(s\text{-}h)}$ and $\gamma_{KT(h\text{-}h)}$ imply that the KT(s-h) and KT(h-h) potentials yield relatively more rigid *a*-SiO_2 phases that suppress lattice distortion.

We constructed small interface models of varying interface O coverage ratio with CRN-MMC simulations using the three VFF models and evaluated their accuracy in reproduction of Si(001)/*a*-SiO_2 interface energetics by comparison with DFT results. Overall, KT(s-h) and KT(h-h) provide reasonable agreement with DFT, whereas KT(h-s) yields consistently smaller $\Delta\tilde{E}_{\text{strain}}$ values (per interfacial unit area) relative to KT(s-h), KT(h-h), and DFT calculations; KT(h-s) strain underestimation in the *a*-SiO_2 region is attributed to the soft parameterization of the oxide phase.

We proceeded to generate four independent sequences of varying O coverage ratio for larger supercells to provide statistical characterization of the interface structures. We compared the structural parameters resulting from various VFF parameterizations in terms of bond angle, ring size, and suboxide distributions; lateral Si-O-Si bridge bond interface densities; and strain energy profiles along [001]. Relative to KT(h-s), the energetically more reliable KT(s-h) and KT(h-h) potentials generate interfaces with the following characteristics: (1) less distorted *a*-SiO_2 regions with narrower Si-O-Si bond angle distributions and narrower ring size distributions in the oxide phases, (2) more graded interfaces in terms of suboxide distributions, (3) lower interface densities of the Si^{2+} oxidation state, and (4) lower interface densities of lateral Si-O-Si bridge bonds.

We also generated strain energy profiles along [001] using energetic calculations from the three potentials [KT(s-h), KT(h-s), and KT(h-h)] to characterize the interface abruptness of the s-h/h-h models (graded interfaces) and the h-s model (abrupt interface). A fourth interface model structure, s-h*, was generated with the KT(s-h) potential and constrained MC simulations to represent an ideally abrupt interface where all interface Si atoms are Si^{2+}. We found that $\Delta\hat{E}_{\text{strain}}$ (per Si atom) is notably lower for the KT(h-s) potential relative to either the KT(s-h) or KT(h-h) potentials. In addition, we observed that $\Delta\hat{E}_{\text{strain}}$ in the oxide regions is notably higher for the more abrupt interfaces (h-s and s-h*) relative to the graded interfaces (s-h and h-h) with KT(s-h) and KT(h-h) calculations, while KT(h-s) calculations exhibit little $\Delta\hat{E}_{\text{strain}}$ variation in the oxide region regardless of the interface model. These results corroborate that the soft parameterization of the oxide phase for KT(h-s) calculations is overly insensitive to structural distortion. Collectively, all three energetic calculations generated strain profiles along [001] that confirm

lower $\Delta\hat{E}_{\text{strain}}$ values in the *c*-Si regions paired with higher $\Delta\hat{E}_{\text{strain}}$ values in the *a*-SiO_2 regions for the abrupt interfaces (h-s and s-h*) relative to the graded interfaces (s-h and h-h). The broader suboxide distributions of the graded s-h interface models generally show the best agreement with experimental results, while the higher strain observed in the Si phase of the s-h models is supported by ion scattering measurements.

Our simulation results suggest that no single parameter set can treat all feasible variants of the diverse Si/SiO_2 system with sufficient parity. Even the orientation of the crystalline Si phase likely requires optimization of the Si rigidity with inevitable effects anticipated for the resultant interface structure. Overall, this study reveals the importance of force field parameter optimization, both in isolated bulk phases and combined to assess relative rigidities, for accurate structural description of interfaces to provide a reliable foundation for studying material properties. The present VFF model could further be improved by taking into account additional penalty energy terms associated with possible coordination defects (such as divalent/trivalent Si and monovalent O defects) to address their effects on the structural properties and energetics. Moreover, by reoptimizing the force parameters the simple valence bond model can be applied to study the mechanical, thermal and vibrational properties of various Si/SiO_2 composite systems.

While the CRN-MMC approach with a simple VFF model is designed to determine thermodynamically equilibrated configurations, the structure of Si/SiO_2 composites can be often a function of process condition, for instance, during Si oxidation and SiO_2 deposition on Si; in those cases, not only thermodynamic equilibrium but also kinetics might need to be considered. To take into account the kinetic effect, it would be necessary to use more advanced methods such as molecular dynamics with a more sophisticated potential model.

ACKNOWLEDGMENTS

We acknowledge National Science Foundation (CBET-0933557) and Robert A. Welch Foundation (F-1535) for their financial support. S. Lee is grateful for the scholarship from the Donald D. Harrington Fellows Program. We would also like to thank the Texas Advanced Computing Center for use of their computing resources.

[1]L. Tsetseris and S. T. Pantelides, Phys. Rev. Lett. **97**, 116101 (2006).
[2]B. E. Deal and A. S. Grove, J. Appl. Phys. **36**, 3770 (1965).
[3]S. Pantelides and M. Long, *Proc. Int. Conf. on the Physics of SiO_2 and its Interfaces*, edited by S. T. Pantelides, p. 339 (Pergamon, New York, 1978).
[4]S. C. Witczak, J. S. Suehle, and M. Gaitan, Solid-State Electron. **35**, 345 (1992).
[5]A. Stesmans and V. V. Afanas'ev, J. Phys.: Condens. Matter **10**, L19 (1998).
[6]A. C. Diebold, D. Venables, Y. Chabal, D. Muller, M. Weldon, and E. Garfunkel, Mater. Sci. Semicond. Process. **2**, 103 (1999).
[7]N. Nagashima, Jpn. J. Appl. Phys. **9**, 879 (1970).
[8]H. Akatsu, Y. Sumi, and I. Ohdomari, Phys. Rev. B **44**, 1616 (1991).
[9]G. Lucovsky and J. C. Phillips, J. Phys.: Condens. Matter **16**, S5139 (2004).
[10]L. C. Feldman, L. Stensgard, P. J. Silverman, and T. E. Jackman, *Proc. Int. Conf. on the Physics of SiO_2 and its Interfaces*, edited by S. T. Pantelides, p. 344 (Pergamon, New York, 1978).
[11]D. A. Muller T. Sorsch, S. Moccio, F. H. Baumann, K. Evans-Lutterodt, and G. Timp, Nature. **399**, 758 (1999).
[12]K. T. Queeney, M. K. Weldon, J. P. Chang, Y. J. Chabal, A. B. Gurevich, J. Sapjeta, and R. L. Opila, J. Appl. Phys. **87**, 1322 (2000).
[13]K. Kimura and K. Nakajima, Appl. Surf. Sci. **216**, 283 (2003).
[14]A. R. Chowdhuri, D.-U. Jim, and C. G. Takoudis, Thin Solid Films **457**, 402 (2004).
[15]F. Rochet, Ch. Poncey, G. Dufour, H. Roulet, C. Guillot, and F. Sirotti, J. Non-Cryst. Solids **216**, 148 (1997).
[16]J. H. Oh, H. W. Yeom, Y. Hagimoto, K. Ono, M. Oshima, N. Hirashita, M. Nywa, A. Toriumi, and A. Kakizaki, Phys. Rev. B **63**, 205310 (2001).
[17]E. A. Irene, E. Tierney, and J. Angilello, J. Electrochem. Soc. **129**, 2594 (1982); E. A. Irene, J. Appl. Phys. **54**, 5416 (1983); E. A. Taft, J. Appl. Phys. **125**, 968 (1978); E. A. Irene, D.W. Dong, and R. J. Zeto, J. Electrochem. Soc., **127**, 396 (1980).
[18]E. H. Poindexter, P. Caplan, B. Deal, and R. Razouk, J. Appl. Phys. **52**, 879 (1981).
[19]R. Helms and E. H. Poindexter, Rep. Prog. Phys. **83**, 2449 (1998).
[20]H. Fukuda, M. Yasuda, T. Iwabuchi, S. Kaneko, T. Ueno, and I. Ohdomari, J. Appl. Phys. **72**, 1906 (1992).
[21]R. Buczko, S. J. Pennycook, and S. T. Pantelides, Phys. Rev. Lett. **84**, 943 (2000).
[22]A. Pasquarello, M. S. Hybertsen, and R. Car, Nature (London) **396**, 58 (1998); A. Pasquarello, M. S. Hybertsen, and R. Car, Phys. Rev. Lett. **74**, 1024 (1995); A. Pasquarello, M. S. Hybertsen, and R. Car, Appl. Phys. Lett. **68**, 625 (1996); A. Pasquarello, M. S. Hybertsen, and R. Car, Phys. Rev. B **53**, 10942 (1996).
[23]K. Tatsumura, T. Watanabe, D. Yamasaki, T. Shimura, M. Umeno, and I. Ohdomari, Phys. Rev. B **69**, 085212 (2004); K. Tatsumura, T. Watanabe, D. Yamasaki, T. Shimura, M. Umeno, and I. Ohdomari, Jpn. J. Appl. Phys., Part 1 **42**, 7250 (2003); K. Tatsumura, T. Watanabe, D. Yamasaki, T. Shimura, M. Umeno, and I. Ohdomari, Jpn. J. Appl. Phys., Part 1 **43**, 492 (2004); T. Watanabe, H. Fujiwara, H. Noguchi, T. Hoshino, and I. Ohdomari, Jpn. J. Appl. Phys., Part 2 **38**, L366 (1999); T. Watanabe, K. Tatsumura, and I. Ohdomari, Appl. Surf. Sci. **237**, 125 (2004).
[24]A. C. T. van Duin, A. Strachan, S. Stewman, Q. Zhang, X. Xu, and W. A. Goddard, J. Phys. Chem. A **107**, 3803 (2003).
[25]Y. Tu and J. Tersoff, Phys. Rev. Lett. **84**, 4393 (2000).
[26]K. O. Ng and D. Vanderbilt, Phys. Rev. B **59**, 10132 (1999).
[27]L. Kong and L. J. Lewis, Phys. Rev. B **77**, 085204 (2008).
[28]W. H. Zachariasen, J. Am. Chem. Soc. **54**, 3841 (1932).
[29]F. Wooten, K. Winer, and D. Weaire, Phys. Rev. Lett. **54**, 1392 (1985).
[30]S. Lee and G. S. Hwang, Phys. Rev. B **77**, 085210 (2008); S. Lee and G. S. Hwang, Phys. Rev. B **78**, 045204 (2008); S. Lee, R. J. Bondi, and G. S. Hwang, Mol. Simul. **35**, 867 (2009); S. Lee and G. S. Hwang, Phys. Rev. B **78**, 125310 (2008); S. Lee, R. J. Bondi, and G. S. Hwang, Phys. Rev. B **80**, 245209 (2010).
[31]S. Dreiner, M. Schürmann, and C. Westphal, Phys. Rev. Lett. **93**, 126101 (2004).
[32]S. Lee, R. J. Bondi, and G. S. Hwang (unpublished).
[33]G. Kresse and J. Furthmuller, *VASP the Guide* (Vienna University of Technology, Vienna, 2001).
[34]J. P. Perdew and Y. Wang, Phys. Rev. B **45**, 13244 (1992).
[35]D. Vanderbilt, Phys. Rev. B **41**, 7892 (1990).
[36]D. R. Hamann, Phys. Rev. B **61**, 9899 (2000).
[37]D. Yu, S. Lee, and G. S. Hwang, J. Appl. Phys. **102**, 084309 (2007).
[38]A. Bongiorno and A. Pasquarello, Phys. Rev. B **62**, R16326 (2000).
[39]Y. Tu, J. Tersoff, G. Grinstein, and D. Vanderbilt, Phys. Rev. Lett. **81**, 4899 (1998).
[40]S. von Alfthan, A. Kuronen, and K. Kaski, Phys. Rev. B **68**, 073203 (2003).
[41]V. M. Burlakov, G. A. D. Briggs, A. P. Sutton, and Y. Tsukahara, Phys. Rev. Lett. **86**, 3052 (2001).
[42]Y. Tu and J. Tersoff, Phys. Rev. Lett. **89**, 086102 (2002).
[43]G. Hadjisavvas and P. C. Kelires, Phys. Rev. Lett. **93**, 226104 (2004).
[44]R. J. Bondi, S. Lee, and G. S. Hwang, Phys. Rev. B **81**, 195207 (2010).
[45]M. Szabadi and P. Hess, Phys. Rev. B **58**, 8941 (1998).
[46]D. M. Follstaedt, J. A. Knapp, and S. M. Myers, J. Mater. Res. **19**, 338 (2004).
[47]K. Laaziri, S. Roorda, and J. M. Baribeau, J. Non-Cryst. Solids **191**, 193 (1995).

[48]J. Sarnthein, A. Pasquarello, and R. Car, Phys. Rev. Lett. **74**, 4682 (1995).
[49]J. P. Rino, I. Ebbsjö, R. K. Kalia, A. Nakano, and P. Vashishta, Phys. Rev. B **47**, 3053 (1993).
[50]A. Bongiorno, A. Pasquarello, M. S. Hybertsen, and L. C. Feldman, Phys. Rev. Lett. **90**, 186101 (2003).
[51]Properties of Silicon EMIS Data Reviews Series No. 4, p. 14 (INSPEC, London, 1988).
[52]N. Ono, K. Kitamura, K. Nakajima, and Y. Shimanuki, Jpn. J. Appl. Phys. **39**, 368 (2000).
[53]T. Rouxel, J. Am. Ceram. Soc. **90**, 3019 (2007).
[54]H. Ni, X. Li, and H. Gao, Appl. Phys. Lett. **88**, 043108 (2006).
[55]C. Tsou, Y. S. Huang, and H. C. Chang, NSTI Nanotechnology Conference and Trade Show, Anaheim, CA, May 2005, **3**, 339–342.
[56]B. Bhushan, *Handbook of Nanotechnology*, p. 773 (Springer, Berlin, 2004).
[57]X. Li, B. Bhushan, K. Takashima, C.-W. Baek, and Y.-K. Kim, Ultramicroscopy **97**, 481 (2003).
[58]K. Laaziri, S. Kycia, S. Roorda, M. Chicoine, J. L. Robertson, J. Wang, and S. C. Moss, Phys. Rev. B **60**, 13520 (1999).
[59]F. Mauri, A. Pasquarello, B. G. Pfrommer, Y.-G. Yoon, and S. G. Louie, Phys. Rev. B **62**, R4786 (2000).
[60]H. I. Liu, D. K. Biegelsen, F. A. Ponce, N. M. Johnson, and R. F. W. Pease, Appl. Phys. Lett. **64**, 1383 (1994).
[61]H. Ohta, T. Watanabe, and I. Ohdomari, Jpn. J. Appl. Phys. **46**, 3277 (2007).
[62]S. R. Billeter, A. Curioni, D. Fischer, and W. Andreoni, Phys. Rev. B. **73**, 155329 (2006).